THE JOURNAL OF BIOLOGICAL CHEMISTRY VOL. 286, NO. 7, pp. 5347–5358, February 18, 2011

Ligand Migration in the Apolar Tunnel of *Cerebratulus lacteus* Mini-Hemoglobin*

Received for publication, July 27, 2010, and in revised form, November 16, 2010 Published, JBC Papers in Press, December 8, 2010, DOI 10.1074/jbc.M110.169045

Alessandra Pesce[‡], Marco Nardini[§], Sylvia Dewilde[¶], Luciana Capece[‖1], Marcelo A. Martí[‖2], Sonia Congia[‡3], Mallory D. Salter[4], George C. Blouin[**4,5], Darío A. Estrin[‖2], Paolo Ascenzi[‡‡], Luc Moens[¶], Martino Bolognesi[§], and John S. Olson[**6]**

*From the [‡]Department of Physics, University of Genova, Via Dodecaneso 33, 16146 Genova, Italy, the [§]Dipartimento di Scienze Biomolecolari e Biotecnologie, Universita' di Milano, Via Celoria 26, 20133 Milano, Italy, the [¶]Department of Biomedical Sciences, University of Antwerp, Universiteitsplein 1, B-2610 Antwerp, Belgium, the [‖]Departamento de Química Inorgánica, Analítica y Química Física/INQUIMAE-CONICET, Facultad de Ciencias Exactas y Naturales, Universidad de Buenos Aires, Ciudad Universitaria, Buenos Aires C1428EHA, Argentina, the **Department of Biochemistry and Cell Biology, Rice University, Houston, Texas 77005-1892, and the [‡‡]Department of Biology and Interdepartmental Laboratory for Electron Microscopy, University Roma Tre, Viale Guglielmo Marconi 446, 00146 Roma, Italy*

The large apolar tunnel traversing the mini-hemoglobin from *Cerebratulus lacteus* (CerHb) has been examined by x-ray crystallography, ligand binding kinetics, and molecular dynamic simulations. The addition of 10 atm of xenon causes loss of diffraction in wild-type (wt) $CerHbO_2$ crystals, but Leu-86(G12)Ala $CerHbO_2$, which has an increased tunnel volume, stably accommodates two discrete xenon atoms: one adjacent to Leu-86(G12) and another near Ala-55(E18). Molecular dynamics simulations of ligand migration in wt CerHb show a low energy pathway through the apolar tunnel when Leu or Ala, but not Phe or Trp, is present at the 86(G12) position. The addition of 10–15 atm of xenon to solutions of wt CerHbCO and L86A CerHbCO causes 2–3-fold increases in the fraction of geminate ligand recombination, indicating that the bound xenon blocks CO escape. This idea was confirmed by L86F and L86W mutations, which cause even larger increases in the fraction of geminate CO rebinding, 2–5-fold decreases in the bimolecular rate constants for ligand entry, and large increases in the computed energy barriers for ligand movement through the apolar tunnel. Both the addition of xenon to the L86A mutant and oxidation of wt CerHb heme iron cause the appearance of an *out* Gln-44(E7) conformer, in which the amide side chain points out toward the solvent and appears to lower the barrier for ligand escape through the E7 gate. However, the observed kinetics suggest little entry and escape (≤25%) through the E7 pathway, presumably because the *in* Gln-44(E7) conformer is thermodynamically favored.

Although molecular dynamics (MD)[7] simulations suggest multiple interior pathways for O_2 entry into and exit from globins, most experiments with mammalian myoglobins (Mbs) and hemoglobins (Hbs) suggest a well defined single pathway involving a short channel between the heme propionates and the heme iron atom that is gated by the distal E7 histidine (1). To search for and define an interior ligand migration trajectory, we chose to use the neuronal mini-hemoglobin from *Cerebratulus lacteus* as a model globin system to examine its long apolar tunnel that leads from the distal portion of the heme pocket to an exit point between the C-terminal regions of the E and H helices of the tertiary fold, a pathway that is roughly 180° opposite the E7 channel and appears to be a major route for ligand entry (2). This model globin provides a well defined system to examine both experimentally and theoretically the effects of xenon binding, mutagenesis, and conformational heterogeneity on the competition between movement through the E7 gate *versus* an internal apolar pathway.

Nerve tissue Hbs occur in both vertebrates and invertebrates (3). Among these, the nerve Hb from the nemertean worm *C. lacteus* (CerHb) is the smallest functional globin known, being composed of 109 amino acids instead of the ~140–160 residues typical of most monomeric globins (4, 5). Analysis of the three-dimensional structure of CerHb has shown a markedly edited 3-over-3-globin fold with deletion of

* This work was supported, in whole or in part, by National Institutes of Health Grants GM035649 and HL047020 (to J. S. O.). This work was also supported by grants from the Italian Ministry of University and Scientific Research (FIRB Project "Biologia Strutturale," RBLA03B3KC) and from the University of Milano (to M. B.), Universidad de Buenos Aires Grants 08-X625 (to M. A. M.) and X076 (to D. A. E.), Agencia de Promocion Cientifica y Tecnologica Grants 07-1650 (to M. A. M.) and 06-25667 (to D. A. E.), Consejo Nacional de Investigaciones Científicas y Técnicas Grant PIP 5218 and a Guggenheim Foundation fellowship (to D. A. E.), and Robert A. Welch Foundation Grant C-0612 (to J. S. O.).

The atomic coordinates and structure factors (codes 2xkg, 2xkh, and 2xki) have been deposited in the Protein Data Bank, Research Collaboratory for Structural Bioinformatics, Rutgers University, New Brunswick, NJ (http://www.rcsb.org/).

[1] Holds a Consejo Nacional de Investigaciones Científicas y Técnicas Ph.D. fellowship.

[2] Members of Consejo Nacional de Investigaciones Científicas y Técnicas.

[3] Present address: Dept. of Neuroscience and Brain Technologies, Italian Institute of Technology Genova, Italy.

[4] Supported by traineeships from the Houston Area Molecular Biophysics Predoctoral National Institutes of Health Training Grant GM008280.

[5] Present address: Optical Technology Division, Biophysics Group, National Institute of Standards and Technology, Gaithersburg, MD 20899-1070.

[6] To whom correspondence should be addressed: Dept. of Biochemistry and Cell Biology, Rice University, 6100 Main St., Houston, TX 77005-1892. Tel.: 713-348-4762; Fax: 713-348-5154; E-mail: olson@rice.edu.

[7] The abbreviations used are: MD, molecular dynamics; Hb, hemoglobin; Mb, myoglobin; CerHb, *C. lacteus* hemoglobin; $CerHbO_2$, oxygenated CerHb; r.m.s.d, root mean square deviation; MSMD, multiple steered molecular dynamics; wt, wild-type.

the N-terminal A-helix, extension of the GH region, and reduction of the C-terminal H-helix (6). Both sequence and fold comparisons indicate that CerHb is equally distant from all known globins, suggesting a specific mini-Hb family within the Hb superfamily. The affinity of CerHb for O_2 is very similar to that of mammalian Mbs, and its function appears to be O_2 storage and then release to axons and brain tissue during periods of burrowing under anoxic conditions (5). The evolution of a storage function in a highly altered globin structure has made CerHb an excellent model for testing biophysical mechanisms involved in the regulation of O_2 affinity and reaction rates (2, 7–10).

Several distinct structural features make CerHb of interest for understanding structure-function relationships. First, the distal portion of the heme pocket contains Tyr-11(B10) and Gln-44(E7), which stabilize heme-bound O_2 by hydrogen bonding in many invertebrate globins with high O_2 affinity (11). However, unlike most of the globins containing this Tyr-Gln motif, CerHb also contains a polar Thr-48 residue at the E11 position, which in most globins is Val, Leu, Ile, or Phe. In CerHb, the non-bonded electrons of the Thr-48(E11) Oγ atom "pull" the proton on the Tyr-11(B10) hydroxyl group away from heme-bound O_2, causing marked 1000- to 100-fold increases in the rate and equilibrium constants for O_2 dissociation, respectively (6, 9). The net result is a P_{50} for O_2 binding of ~0.6 torr (K_d~ 1 μM) for CerHb, which is similar to that of mammalian Mbs (10).

The second unusual structural feature of CerHb is a long apolar tunnel that connects the heme pocket to solvent through an exit pore between the C-terminal ends of the E and H helices. This tunnel is correlated with an unusually large association rate constant for O_2 binding to CerHb (k'_{O_2} = 230 $\mu M^{-1}s^{-1}$) when compared with those of other invertebrate globins containing the Tyr-Gln active site motif, which normally show bimolecular association rate constants on the order of 1–5 $\mu M^{-1}s^{-1}$ (11). The rate constant for O_2 binding to CerHb is 10 times larger than that for sperm whale Mb and is similar to those for His(E7)Gly[8] mutants of Mbs and Hbs and to unhindered pentacoordinate model hemes (12–14). The cause of these high rates appears to be a wide, ~10 Å long channel that traverses the interior of the globin matrix, allowing relatively unhindered access to the heme pocket.

The CerHb tunnel has roughly the shape of an hourglass, is located between the E- and H-helices, is directed from the solvent to the heme pocket, and terminates at the active site as an aperture, which is circumscribed by the side chains of Val-7(B6), Phe-10(B9), and Thr-48(E11). This channel is lined by small hydrophobic residues and has a diameter that varies from 6.9 to 5.5 Å at the narrowest segment, which is close to residue Leu-86(G12) (6). Diatomic ligands are thought to enter and exit the tunnel through an opening between the E and H helix, which appears to have evolved by the complete loss of the N-terminal A-helix that is found in almost all other globins. Obstructing the tunnel entrance by increasing the size of Ala-55(E18) to Phe or Trp causes an ~4-fold decrease of both k'_{O_2} and k_{O_2} and a 5-fold increase in the fraction of geminate recombination due to restriction of both entry into and escape from the apolar channel (2). In contrast, mutagenesis of Gln-44(E7) to either smaller or larger amino acids has little effect on internal rebinding after photolysis or bimolecular binding from solvent, suggesting strongly that the E7 gate for ligand entry/exit found in mammalian Hbs and Mbs (13, 14) is not a significant pathway in CerHb (2).

Apolar cavities and tunnel systems that could support ligand diffusion to and from the heme have been observed in selected globin families, although relative to CerHb, some of these channels are structurally and topologically distinct within the overall tertiary fold (15–17). However, in most cases there has been little experimental proof that these tunnels are used by diatomic ligands. Cavities large enough to accommodate xenon atoms have been found in most globins, including sperm whale Mb and *Scapharca inaequivalvis* HbI; however, in both of the latter cases, xenon binding has little effect on either the fraction of geminate recombination or on overall rates of ligand binding or release (13, 18, 19), implying that these internal spaces are not part of the route for ligand entry and escape.

In this work we have focused our attention on providing both direct experimental and theoretical evidence for ligand access to the heme pocket through the tunnel in CerHb and estimates of what fraction of the ligands use this route *versus* the E7 gate pathway, which dominates in mammalian Mbs and Hbs that contain a distal histidine. We have shown that xenon atoms can be accommodated within the CerHb tunnel by x-ray crystallography, examined the effects of xenon binding on CO geminate recombination, measured the effects of changing the width of the channel with Leu-86(G12) to Ala, Phe, and Trp mutations, and complemented these experiments with molecular dynamics simulations of how Leu-86 mutations modulate the tunnel shape, size, and energy barriers to ligand migration. Our results demonstrate that there is a strong correlation between tunnel size and observed rates of ligand binding to CerHb. More importantly, CerHb is the first example of a globin in which xenon binding markedly increases geminate recombination and slows bimolecular ligand entry.

EXPERIMENTAL PROCEDURES

Sample Preparation—Wild-type (wt) and mutant recombinant CerHbs were expressed and purified as described previously using a synthetic gene with codon usage optimized for expression in *Escherichia coli* (6, 10). Most recombinant CerHb samples were isolated in the reduced state and used directly. When necessary, the unstable mutants were pre-reduced with dithionite, quickly passed through a Sephadex G-25 column, and eluted with buffer equilibrated with 1 atm of CO. All reactions were measured in 0.1 M phosphate buffer, pH 7.0, 1.0 mM EDTA, 20 °C.

Measurement of Overall Rates of Ligand Association and Dissociation—CO association time courses were measured after complete laser photolysis of 50 μM CerHbCO samples

[8] Mutations are defined by the single letter code for the native amino acid, its sequence position, and the single letter code for the mutant amino acid, *e.g.* Leu-86(G12)→Ala is represented as L86A.

containing various CO concentrations under pseudo first order conditions, and CO dissociation was measured by mixing CerHbCO with high concentrations of NO (2). Time courses for O_2 association and dissociation were measured after complete laser photolysis of CerHbCO samples containing various mixtures of O_2/CO (2), and association rate constants for NO binding to deoxy-CerHb were measured using a flow-flash multi-mixing apparatus and the 500-ns dye laser system (2).

Measurement of Geminate Recombination—Time courses for internal rebinding within CerHb were measured at 436 nm after excitation with a 9-ns excitation pulse from a Lumonics YAG-laser system using a Tektronix TDS3052 digitizing oscilloscope and Hamamatsu high speed PM tube with a 2-ns rise time. Experimental procedures and fitting routines were performed as previously described (2). For experiments with xenon, a 0.3-ml sample of CerHbCO was transferred to a stainless steel pressure cell with a gas volume of ~4 ml. The cell was equipped with anti-reflection-coated sapphire windows and had a path length of 1 mm as previously described (19). Data were first collected with 1 atm CO over the sample, and then the required pressure of xenon was introduced through a three-way valve attached to the top of the cuvette. The sample was then equilibrated with the CO-xenon mixture for several minutes by shaking the cuvette to expose the solution to the gas space. The fraction of geminate recombination (F_{gem}) and the rate of geminate recombination (k_{gem}) were determined as previously described (2).

Crystallization, Data Collection, and Refinement—The oxygenated derivative of the Leu-86(G12)Ala (L86A) CerHb mutant was crystallized by vapor diffusion techniques (protein concentration 27 mg/ml) under conditions matching those for the wt protein (20). Elongated prismatic crystals (about $0.05 \times 0.05 \times 0.2$ mm^3) grew within 1 week. The crystals were transferred to 2.8 M ammonium sulfate, 50 mM sodium acetate, pH 6.0, and 15% glycerol (v/v) (cryoprotectant solution) immediately before data collection at 100 K. L86A CerHbO_2 crystals are isomorphous with those of the wt protein.

High resolution data (1.60 Å) on the L86A CerHb mutant crystals were collected at the European Synchrotron Radiation Facility (beam line ID14-1, Grenoble, France) (Table 1). To promote xenon diffusion within the protein matrix, selected L86A CerHbO_2 crystals in their cryoprotectant solution were exposed to 10 bar xenon for 5 min in a high pressure chamber (Xcell, Oxford Cryo-system). The x-ray diffraction data sets for the xenon-bound oxygenated derivative of the L86A CerHb mutant were collected at 100 K using a MAR-Research 345 imaging plate detector coupled to a Rigaku RU-H3R rotating anode generator (copper $K\alpha$ radiation; resolution 2.3 Å) (Table 1).

High resolution data (1.3 Å) for the aquomet form of the wt CerHb protein crystals were collected at the European Synchrotron Radiation Facility (beam line ID14-1, Table 1). The aquomet form of CerHb was obtained by soaking the oxygenated wt protein crystals (20) with 10 mM $K_3Fe(CN)_6$. Crystals were then transferred to the cryoprotectant solution supplemented with the same amount of $K_3Fe(CN)_6$ before data collection at 100 K.

All diffraction data were processed using MOSFLM and SCALA programs (21, 22) and phased by molecular replacement methods with the program MOLREP (23), as implemented in the CCP4 program package (CCP4, 1994), using the wt CerHbO_2 structure as the starting model (PDB accession code 1kr7) (6). Crystallographic refinement was performed using the program REFMAC (24), and the program COOT (25) was used for model building/inspection. Xenon atoms were initially refined at 100% occupancy together with the protein structure. At the end of refinement, inspection of difference Fourier maps indicated that the xenon occupancies were overestimated. To obtain better values, the fractional occupancies were systematically decreased until no residual difference signal was detected. The relevant data collection and refinement statistics are reported in Table 1. The programs Procheck (26) and Surfnet (27) were used to assess the stereochemical quality of the protein structures and to explore the protein matrix cavities. Atomic coordinates and structure factors for the L86A CerHbO_2, xenon-bound L86A CerHbO_2, and wt aquomet CerHb have been deposited with PDB accession codes 2xkg, 2xkh, and 2xki, respectively (28).

Computational Methods—MD simulations were performed starting from the crystal structure of wt CerHbO_2 (PDB accession code 1kr7 (6)), and in some cases the *out* conformation of Gln-44(E7) observed in the structure of the wt aquomet CerHb derivative was used in the model. All systems were solvated with water molecules leaving 10 Å between the protein surface and the system limit. Histidine protonation was assigned to favor H-bond formation. All simulations were performed with the parmm99 force field (29) using Amber8 (30). The equilibration process was performed by slowly heating the system to a final temperature of 298 K. The oxygenated and deoxygenated heme model system charges were determined by using restrained electrostatic potential charges (31) and HF/6–31G(d) wave functions according to the Amber standard protocol. This set of partial charges has been successfully used in similar systems (32).

To study the properties of the wt CerHb tunnel cavity system, the diffusion free energy profiles for O_2 along the tunnels were calculated by performing constant velocity MSMD simulations using the Jarzynski inequality (33), which relates equilibrium free energy values with the irreversible work performed over the system and proceeds along a reaction coordinate from reactants to products. In the present study the reaction coordinate was chosen as the iron to O_2 distance. Calculations were performed using a force constant of 200 kcal mol^{-1} Å^{-1} and a pulling velocity of 0.05 Å ps^{-1}. To reconstruct the free energy profile of ligand migration along the tunnel, a set of MSMD runs was performed starting from equilibrated MD structures with the ligand (i) in the distal pocket, (ii) in the crystallographic xenon-binding sites, and (iii) outside the tunnel. Ten MSMD simulations were performed in each direction (forward/exit and backward/entry). In cases in which two overlapping profiles were obtained (from entry and exit sets), we confirmed that they matched.

The free energy profiles for the transition between the *in* and *out* conformations of Gln-44(E7) were obtained with Umbrella Sampling techniques (34). In this method the

TABLE 1
Data collection and refinement statistics for L86A CerHbO$_2$ and wild-type aquomet CerHb

	L86A CerHbO$_2$ (PDB 2xkg)	L86A CerHbO$_2$ 10 bar xenon (PDB 2xkh)	wt aquomet CerHb (PDB 2xki)
Data collection parameters			
Space group	$P2_12_12_1$	$P2_12_12_1$	$P2_12_12_1$
Cell dimensions (Å)	a = 42.7	a = 42.9	a = 42.5
	b = 43.4	b = 43.0	b = 43.2
	c = 59.4	c = 59.5	c = 60.2
Resolution (Å)	34.9-1.60	35.0-2.3	35.1-1.37
	(1.69-1.60)	(2.34-2.30)	(1.37-1.30)
Observations	58,823	20,818	156,248
Unique reflections	15,045	5,031	27,887
Completeness (%)	99.7 (100)[a]	97.5 (93.0)	99.9 (100)
R-merge[b] (%)	4.0 (9.5)	8.8 (40.0)	5.1 (34.5)
$I/\sigma(I)$	24.1 (12.7)	8.6 (4.5)	15.5 (3.3)
Multiplicity	3.9 (4.0)	3.5 (3.0)	5.6 (3.9)
Refinement			
R-factor[c]/R-free (%)	15.4/18.6	19.4/26.6	14.4/17.7
Protein atoms in the asymmetric unit	826	817	831
Dioxygen molecules	1	1	
Water molecules	135	61	131
Sulfate ions	3	1	1
Glycerol			1
Model quality			
Overall B-factor (Å^2)	11	17	14
r.m.s.d. from ideal values:			
Bond lengths (Å)	0.011	0.010	0.011
Bond angles (°)	1.172	1.073	1.244
Ramachandran plot[d]:			
Most favored regions (%)	98.1	99.1	100
Additional allowed regions (%)	1.9	0.9	0

[a] Outer shell statistics are shown within parentheses.
[b] R-merge = $\Sigma_h\Sigma_i|I_{hi} - \langle I_h\rangle|/\Sigma_h\Sigma_i I_{hi}$.
[c] R-factor = $\Sigma_H||F_{obs}| - |F_{calc}||/\Sigma|F_{obs}|$, where F_{obs} and F_{calc} are the observed and calculated structure factor amplitudes, respectively.
[d] Data were produced using the program PROCHECK (26).

potential function is modified so that the unfavorable states are sampled sufficiently. The modification of the potential function can be written by adding a bias harmonic potential according to $E'(r) = E(r) + k(r - \xi)^2$, where $E(r)$ is the potential energy of the protein for a given configuration r (*i.e.* the force field equation), and k is the force constant. The harmonic potential is centered at some point along the reaction coordinate (ξ). The corresponding profile was computed using the Gln-44(E7) Nϵ2-iron distance as the selected reaction coordinate, and 12 different 2-ns runs were performed varying the center of the harmonic potential along the reaction coordinate.

In-silico L86A, L86F, and L86W mutant structures were generated using the Modeler program (35). The generated structures were equilibrated by slowly heating the system to a final temperature of 298 K. MD simulations for the *in silico*-generated mutants were performed for 10 ns using the specifications described above. From these simulations we obtained plots representing the interaction energy between the O_2 molecule and the protein determined from classical molecular interaction potential calculations.

RESULTS

Crystal Structures of L86A CerHbO$_2$ and Its Xenon Derivative—To examine the accessibility of the apolar tunnel, wt CerHbO$_2$ crystals were equilibrated with high pressures of pure xenon gas. This gas has been used successfully to identify cavities in a variety of Mbs and Hbs (15, 16, 18, 36–40). Unfortunately, wt CerHbO$_2$ crystals quickly lose diffraction power after exposure to xenon, even at low pressure and short times. This effect could be due to xenon binding at intermolecular crystal contacts, causing disruption of the crystal lattice, or to xenon binding within the apolar channel, expanding the protein and indirectly disrupting intermolecular contacts.

To solve this problem we crystallized the L86A CerHbO$_2$ mutant, in which constriction near the center of the tunnel is relieved by removal of three side chain carbon atoms at the G12 helical position. When crystals of L86A CerHbO$_2$ were exposed to high pressures of xenon, diffraction persisted after incubation with ~10 atm of xenon, and a full diffraction data set was successfully collected at 2.3 Å resolution. The resulting structure was refined to a final R-factor of 19.4% and R-free of 26.6% and compared with the independently determined structure of the xenon-free L86A CerHbO$_2$ mutant. For comparison, a full dataset was collected to 1.6 Å resolution for xenon-free L86A CerHbO$_2$, and a model was refined to final R-factor and R-free values of 15.4 and 18.6%, respectively (Table 1).

The backbone structure of xenon-free L86A CerHbO$_2$ is virtually identical to that of wt CerHbO$_2$, with a r.m.s.d. of 0.15 Å calculated for all 109 Cα atom pairs. The only significant structural differences between the mutant and wt structures are small rotations of the side chains of Leu-98(H9) and Ile-102(H13). The net result of these changes and the Ala replacement is an increase in the tunnel inner diameter by ~1.9 Å. This increase either promotes preferential xenon binding in the channel *versus* binding to external sites or facilitates internal xenon binding without requiring expansion of the protein structure and further alterations in intermolecular packing.

TABLE 2

Distances between polar atoms in the distal pockets of L86A CerHbO$_2$, wild-type CerHbO$_2$, and wild-type aquomet CerHb

The *in* and *out* conformation of the Gln-44(E7) side chain are indicated by the superscript "i" and "o" letters.

	wt CerHbO$_2$ (PDB 1kr7)[a]	Xenon-free L86A CerHbO$_2$ (PDB 2xkg)	Xenon-bound L86A CerHbO$_2$ (PDB 2xkh)	wt aquomet CerHb (PDB 2xki)
Fe—O$_2$ (Å)	1.94	1.97	1.90	
Fe—water (Fe^{3+}) (Å)				2.14
Fe-O1-O$_2$ angle (°)	103	110	−105	
Tyr-11(B10) OH—O$_2$ (Å)	2.57	2.47	2.46	
Tyr-11(B10) OH—water (Fe^{3+}) (Å)				2.87
Gln-44(E7) NE2—O1 (Å)	2.60	2.96		
Gln-44(E7) NE2—O$_2$ (Å)			2.65	
Gln-44(E7) NE2—water (Fe^{3+}) (Å)				2.72^{i}, 7.13^{o}
Tyr-11(B10) OH—Thr-48(E11) OG1 (Å)	2.59	2.62	2.75	2.68
Tyr-11(B10) OH—Gln-44(E7) NE2 (Å)	3.24	3.33	3.41^{i}, 7.97^{o}	3.59
Gln-44(E7) NE2—Thr-48(E11) OG1 (Å)	3.53	3.34	3.48^{i}, 7.50^{o}	3.34
Gln-44(E7) NE2—solvent water (Å)			2.72^{o}	2.83^{o}
Solvent water—Ala-40(E3) O (Å)			2.59^{o}	2.73^{o}

[a] Structure was reported in Pesce *et al.* (6).

TABLE 3

Rate constants for bimolecular and geminate recombination of CO with wild-type and L86A CerHb at pH 7, 20 °C

CerHb	k'_{CO}	$k_{gem,CO}$	$F_{gem,CO}$	$k'_{entry,CO}$
	$\mu M^{-1}s^{-1}$	μs^{-1}		$\mu M^{-1}s^{-1}$
Leu-86(wt)[a]	32 ± 5	80 ± 40	0.05 ± 0.03	640 ± 400
Leu-86(wt) + xenon	26	63 ± 10	0.29 ± 0.5	90
Ala-86	30	≥150, 15	0.13	190
Ala-86 + xenon	27	≥150, 28	0.34	80

[a] The numbers for wt CerHb are based on the average of all determinations for the past 6 years (≥10 separate preparations, see Refs. 5, 8, and 9). The error in k'_{entry} is very large because F_{gem} is close to 0.0, poorly defined, and has an error of ±60%. When F_{gem} is ≥0.1, the error in k'_{entry} diminishes greatly to ~±20%.

The heme cavity of xenon-free L86A CerHbO$_2$ is identical to that of wt CerHbO$_2$ (Table 2). Conservation of the heme distal-site structure in wt CerHbO$_2$ and the xenon-free L86A mutant is supported by their similar kinetic parameters for diatomic ligand binding (Tables 3–5), which ensures that this mutant is a reliable model for studying ligand diffusion through the apolar matrix tunnel. The structure of the L86A mutant containing bound xenon is also very similar to that of wt CerHbO$_2$, with a r.m.s.d of 0.19 Å for all 109 Cα atom pairs. Inspection of the residual difference electron density after the initial refinement of the xenon-bound mutant indicated the presence of two xenon atoms (Xe1 and Xe2) at refined occupancies of ~ 65% and temperature factors of 36 and 22 Å^2, respectively (Fig. 1). The Xe1 site is directly adjacent to Ala-86(G12) and surrounded by the heme ring B vinyl carbon atoms, the terminal side chains of Phe-10(B9) and Ile-52(E15). The Xe2 site is adjacent to the Xe1 site, surrounded by the heme ring B methyl group, Tyr-51(E14), Leu-98(H9), Ala-101(H12), and Ile-102(H13), and is near Ala-55(E18) and the exit to solvent. Together, the xenon atoms fill most of the tunnel located in the protein interior (*transparent gray spaces* in Fig. 1), help define the apolar channel, and are stabilized by favorable van der Waals contacts with Val-7(B6), Phe-10(B9), Thr-48(E11), Tyr-51(E14), Ile-52(E15), Ala-55(E18), Ala-86(G12), Leu-98(H9), Ala-101(H12), and Ile-102(H13).

Unexpectedly, xenon binding to the L86A mutant induces small but detectable changes in the position of the Gln-44(E7) side chain, which alter the hydrogen bonding interactions with bound O$_2$ and the heme propionates (Fig. 2). The second bound O atom rotates outward toward the solvent interface and closer to the terminal O or N atom of Gln-44(E7) (Fig. 2*A*). The B factors for heme-bound O$_2$ ($B_{O(1)}$ = 35 Å^2, $B_{O(2)}$ = 38 Å^2) are higher in the presence of xenon compared with wt CerHb ($B_{O(1)}$ = 23 Å^2, $B_{O(2)}$ = 28 Å^2). In contrast, the B factor averages for the two independent structures are essentially the same, 17 *versus* 15 Å^2, respectively, for the xenon bound L86A *versus* wt CerHbO$_2$. Thus, the difference in mobility and orientation of coordinated O$_2$ appears to be real and coupled to the conformational heterogeneity of Gln-44(E7).

The innermost Gln-44(E7) conformer (*in*) is close enough to stabilize the ligand by hydrogen bonding if the Nϵ atom is near the second bound O atom. The Tyr-11(B10) hydroxyl H atom is still hydrogen-bonded to the Thr-48(E11) hydroxyl O atom, and the non-bonded electrons of the Tyr-11(B10) hydroxyl O atom are still close enough to destabilize heme-bound O$_2$. Thus, the O$_2$ dissociation rate constant is still expected to be large in the xenon-bound mutant, as is observed for both xenon-free L86A and wt CerHbO$_2$.

In the outermost conformation of Gln-44(E7) (*out*) in xenon-bound L86A CerHbO$_2$, the amide side chain has moved toward the solvent and away from the iron atom by a small ~56° rotation about the Cα-Cβ bond, has lost contact with the ligand, and instead is stabilized by a hydrogen bonding network, which links the Nϵ or Oϵ atom to the carbonyl O of Ala-40(E3) and the heme A propionate carboxyl groups through two well defined water molecules (Table 2; Fig. 2*A*).

Similar *in* and *out* conformations for Gln-44(E7) occur in the structure of wt aquomet CerHb (Fig. 2*B*). The terminal amide side chain atoms in the *in* conformation appear to be interacting with the coordinated water molecule, whereas in the *out* conformation the amide side chain has moved away from the coordinated ligand and again is fixed in position by a hydrogen bonding network involving the carbonyl of Ala-40(E3). In both the *in* and *out* conformers of aquomet CerHb, there is an electrostatic interaction between Lys-47(E10) and the heme-7-propionate. In the *out* conformer of both xenon-bound L86A CerHbO$_2$ and wt aquomet CerHb, the Gln-44(E7) amide side chain still blocks access to the iron atom by filling the outer portion of the channel between the N-terminal region of the E-helix and the heme propionates. This position contrasts with the truly *open* position of His(E7) in sperm

TABLE 4
Rate and equilibrium constants for O_2 and CO binding to position 86(G12) and 55(E18) mutants of CerHb at pH 7.0, 20 °C

CerHb	k'_{O_2}	k_{O_2}	K_{O_2}	k'_{CO}	k_{CO}	K_{CO}	K_{CO}/K_{O_2}
	$\mu M^{-1}s^{-1}$	s^{-1}	μM^{-1}	$\mu M^{-1}s^{-1}$	s^{-1}	μM^{-1}	
Ala-55/Leu-86 (wt)[a]	230 ± 17	190 ± 25	1.2 ± 0.2	32 ± 5	0.054 ± 0.005	590 ± 100	490 ± 110
Ala-86	230	153	1.5	30	0.053	570	380
Phe-86	120	71	1.7	24	0.024	710	600
Trp-86	97	60	1.6	16	0.014	1100	700
Trp-55	63	66	0.95	15	0.029	500	520

[a] The numbers for wt CerHb are based on the average of all determinations for the past 6 years (≥10 separate preparations).

TABLE 5
Observed bimolecular rate constants for NO association and calculated rate parameters for ligand entry into 86(G12) and 55(E18) mutants of CerHb at pH 7.0, 20 °C

CerHb	k'_{NO}	$k_{gem,CO}$	$F_{gem,CO}$	$k'_{entry,CO}$
	$\mu M^{-1}s^{-1}$	μs^{-1}		$\mu M^{-1}s^{-1}$
Ala-55/Leu-86(wt)[a]	230 ± 30	80 ± 40	0.05 ± 0.03	640 ± 400
Ala-86	200	≥150, 15	0.13	190
Phe-86	110	≥150, 53	0.17	140
Trp-86	67	~80	0.52	31
Trp-55	45	9.4	0.44	33

[a] The numbers for wt CerHb are based on the average of all determinations for the past 6 years (≥10 separate preparations, see Table 3).

whale MbCO when it is protonated at low pH or when Phe-46(CD4) is mutated to Val (41, 42).

Effects of Xenon Binding on Geminate CO Recombination—As shown in Fig. 3 and Table 3, F_{gem} for both wt and L86A CerHbCO increases almost linearly with increasing xenon pressure, from ~0.1 at 0 atm to ~0.35 at 15 atm (Table 3). Equilibration with 15 atm of N_2 has no effect on F_{gem} for wt CerHbCO, ruling out a non-specific pressure effect. As observed previously for wt MbO_2 (13), there is no effect of 15 atm of xenon on the fraction of geminate CO rebinding in Mb, which remains close to 0 (expected value is 0.05, Fig. 3*B*). The linear dependence of F_{gem} on xenon pressure indicates weak binding of the gas to CerHbCO in solution, with a $P_{50} >$ 15 atm. The fractional occupancy estimated from the crystal structure at 10 atm of xenon was ~0.65, indicating a somewhat higher affinity under the crystallization conditions. Assuming a lower estimate of 15 atm for the P_{50} of both xenon sites, the extent of geminate recombination at full occupancy of sites 1 and 2 is predicted to be ~0.7 compared with ≤0.1 when the channel is completely open. Thus, xenon binding in the channel reduces the extent of CO escape at least 7-fold, strongly supporting the view that the apolar channel is the major pathway for ligand escape. It should be noted that the results in Fig. 3 are the first to show a large effect of xenon binding on the total fraction of geminate recombination in a globin.

Effects of L86A, L86F, and L86W Mutations—We have already examined the effects of increasing the size of the amino acid at the Ala-55(E18) position, which is adjacent to the Xe2 site, and found that Leu, Phe, and Trp substitutions trap CO in the tunnel after laser photolysis, increasing F_{gem} to ~0.50, and decreasing the bimolecular rate constant for ligand entry roughly 4–10-fold (Fig. 4). To examine the Xe1 site, we measured ligand binding to L86A, L86F, and L86W mutants (Figs. 4 and 5; Tables 4 and 5).

The L86F and L86W CerHbCO mutants show progressive increases in geminate recombination, with F_{gem} for the L86W mutant being roughly the same as that for the A55W variant. However, for the 86(G12) mutants, the rates of geminate recombination remain very large, ≥100 μs^{-1} compared with that for the A55W mutant, which is 10-fold smaller, ~10 μs^{-1} (Fig. 4). The Trp-86(G12) side chain keeps the photodissociated ligand closer to the iron atom, facilitating its rebinding and lowering the entropic barrier to bond reformation. In the A55W mutant, the entire tunnel is available to dissociated ligands because only the exit to solvent is blocked, and as a result, rebinding to the heme iron is slower (2).

The rates of O_2 and CO binding to the 86 mutants are compared with those for wt and A55W CerHb in Table 4, and a summary of NO association and calculated bimolecular rates of ligand entry are presented in Fig. 5 and Table 5. Both the association and dissociation rate constants for O_2 binding decrease 2–3-fold when Leu-86 is replaced with Trp, demonstrating that the indole ring limits both diatomic gas escape and entry into the active site but has little effect on the overall affinity. A similar ~3-fold decrease in k'_{NO} is observed. Because of the free-radical nature of NO, its reactivity with reduced iron is intrinsically very high, and virtually every NO molecule that enters the active site binds, causing ligand movement into the distal portion of the heme pocket to be the rate-limiting step. Thus, k'_{NO} should equal the bimolecular rate of ligand entry, k'_{entry}.

The lower reactivities of O_2 and CO cause them to enter and leave the active site many times before bond formation occurs, and for a two-step scheme the overall association rate constant is given by Equation 1 (2),

$$k'_{ligand} = k'_{entry}\left(\frac{k_{bond}}{k_{bond} + k_{escape}}\right) = k'_{entry}(1 - F_{gem}) \quad \text{(Eq. 1)}$$

where k_{bond} and k_{escape} are the first order rates for internal iron-ligand bond formation and ligand escape, respectively. Thus, k'_{entry} can be estimated from the overall association rate constant and the corresponding fraction of geminate recombination. Unfortunately, geminate rebinding of O_2 to CerHb is very fast, and a significant amount occurs during the excitation pulse, making an accurate estimate of F_{gem,O_2} difficult (2). Estimates of k'_{entry} based on bimolecular association rate constants and F_{gem} values for CO binding are given in Tables 3 and 5.

Equilibrating L86A CerHb with 15 atm of xenon causes an ≥2-fold decrease in the value of k'_{entry}. Assuming that the two xenon sites are ≤50% occupied, this result suggests that filling the Xe1 and Xe2 pockets would decrease k'_{entry} at > 4-fold. Similarly, the L86W mutation decreases the calculated k'_{entry} value ~6-fold compared with the computed value for

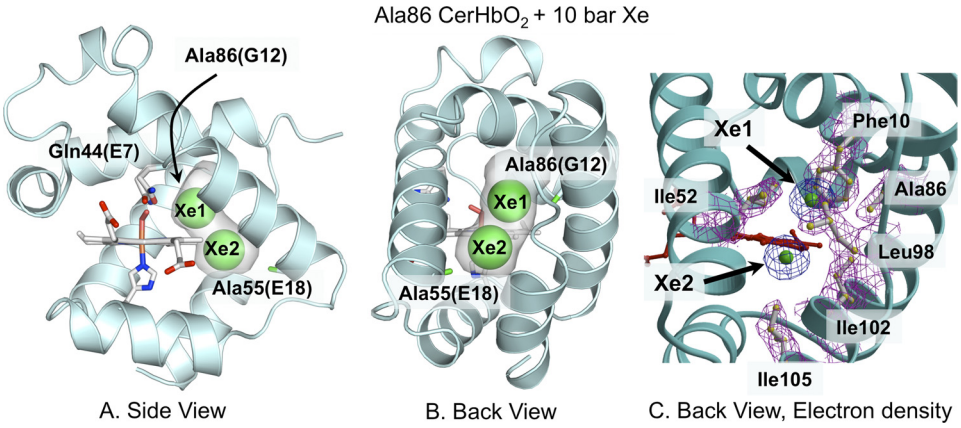

FIGURE 1. **Effects of 10 atm of xenon on the structure of L86A CerHbO$_2$ (PDB code 2xkh).** *A*, side view looking through the heme propionates into the protein interior. *B*, back view looking between the E and H helices through the apolar tunnel. The empty space in the tunnel is *highlighted in gray*. The heme group, proximal His, and Gln-44(E7) are shown as *sticks* with O atoms in *red*, N atoms in *blue*, and C atoms in *white*. The xenon atoms are shown as *green spheres* at half their van der Waals radii to indicate partial occupancy and designated as Xe1 and Xe2. The Ala-86(G12) and Ala-55(E18) methyl side chains are shown as *green sticks*. *C*, electron density map of the amino acids and xenon atoms lining the tunnel using the same orientation as in *panel B* are shown. Amino acid side chains are shown as *ball and stick models*, and the xenon atoms are drawn as *green spheres*. The electron densities ($2F_o - F_c$ map contoured at 1σ) are shown in *magenta* for the side chains and in *blue* for the xenon atoms.

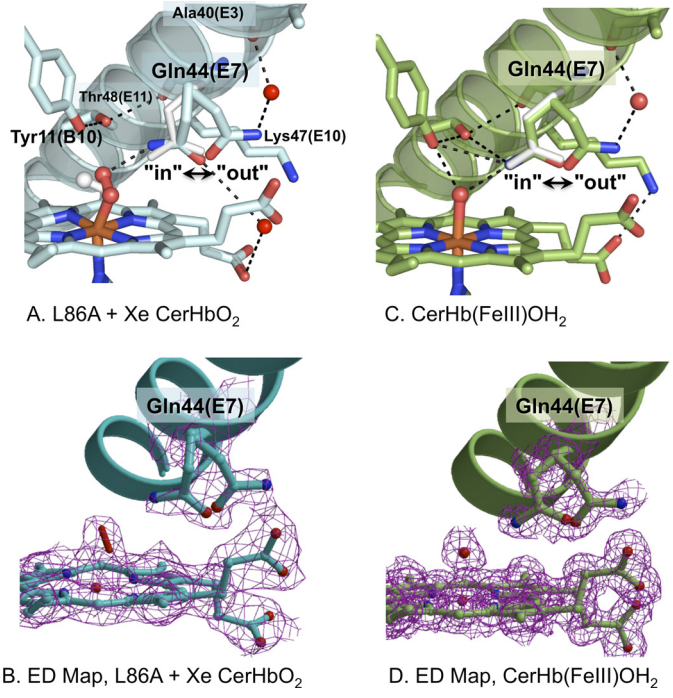

FIGURE 2. **Multiple conformations of Gln-44(E7) in various structures of CerHb.** *A*, distal pocket, E-helix, multiple conformations of Gln-44(E7), and bound O_2 of xenon-bound L86A CerHbO$_2$ (2xkh, *cyan*). *B*, the electron density map ($2F_o - F_c$ map contoured at 1σ) for xenon-bound L86A CerHbO$_2$ is shown in *magenta* for the double conformation of Glu-44(E7), the heme group, and the oxygen molecule coordinated to the iron atom and for the Gln-44(E7) side chain refined in two (*in* and *out*) conformations. *C*, heme pocket, E-helix, in and out conformers of Gln-44(E7), and coordinated water of wt aquomet CerHb (2xki, *green*). *D*, electron density map ($2F_o - F_c$ map contoured at 1σ) for wt aquomet CerHb are shown in *magenta* for the heme group, the heme-coordinated water molecule, and for the Gln-44(E7) side chain refined in two (*in* and *out*) conformations. In the *upper panels A* and *C*, the Gln-44(E7) side chain conformer from wt CerHbO$_2$ (1kr7) is superimposed as *white sticks*. The position of bound O_2 in wt CerHbO$_2$ is also shown in *panel A* as *white sticks*. Residues Tyr-11(B10), Gln-44(E7), Lys-47(E10), and Thr-48(E11) are represented as *sticks*; heme-bound O_2 and coordinated H_2O are represented as *red sticks*; the heme group is displayed as *sticks* with the carbon atoms either *light blue* (*panel A*) or *green* (*panel B*), the iron atom in *orange*, and nitrogen and oxygen atoms in *blue* and *red*, respectively; external water molecules are displayed as *red spheres*; hydrogen bonds are drawn as *dashed black lines*.

L86A CerHb. The magnitude of this decrease is similar to that observed for the A55W mutation (Table 5).

Dynamics of O_2 Entry/Exit for wt CerHb and the Leu-86(G12) Mutants—To analyze the resistance to ligand migration through the xenon sites, we computed the free energy profile for O_2 movement through the apolar tunnel in wt CerHbO$_2$ (PDB accession code 1kr7 (6)). The free energy profile and positions of the O_2 molecule as it was moved along the tunnel are presented in Fig. 6. After entry into the channel, a small barrier was observed between 8 and 11 Å from the heme-iron atom, with two well-separated local minima (Fig. 6*A*). This barrier is the result of steric restriction of the tunnel diameter by the Leu-86(G12) side chain in wt CerHb. The O_2 positions in Fig. 6*B* show that the ligand can pass consecutively through both xenon sites, which tentatively correlate with the observed free energy minima. Much larger free energy barriers were calculated on the two ends of the broad free energy well of the tunnel. A barrier of ~5.5 kcal/mol was computed for O_2 movement from the distal pocket into the Xe1 binding site, and then a ~2 kcal/mol barrier was estimated for ligand movement out of the Xe2 site, past Ala-55(E18), and into solvent. The 5.5 kcal/mol barrier is due to steric restrictions of the side chains of Phe-10(B9), Tyr-11(B10), and Val-7(B6) (Fig. 6*B*).

To complement the kinetic results in Tables 4 and 5, we constructed the L86A, L86F, and L86W mutants *in silico*, performed 10-ns MD simulations, analyzed the tunnel structure for each of them, and displayed the results in Fig. 7. The L86A mutant displays a continuous tunnel with two secondary sites corresponding to the Xe1 and Xe2 positions. In contrast, the L86F and L86W mutants display a marked increase of the barrier between the Xe1 and Xe2 free energy wells shown in Fig. 6*A* and create spatial barriers that divide the tunnel into separate cavities as shown in Figs. 7, *B* and *C*. Blockage of the tunnel by these aromatic side chains is consistent with the 2–5-fold decreases in the rates of ligand binding and release and the increase in $F_{gem,CO}$ observed for these mutants (Fig. 5 and Tables 4 and 5). However, the kinetic results suggest that

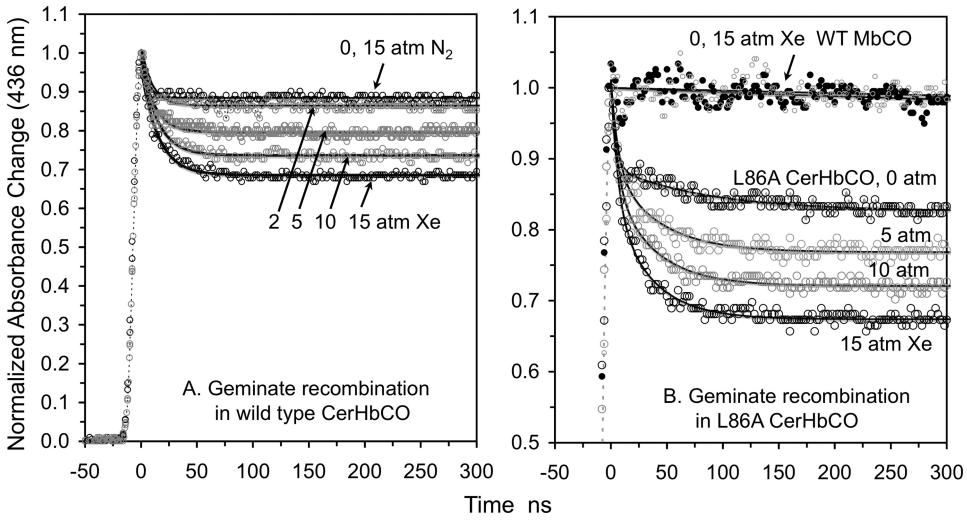

FIGURE 3. **Effect of xenon on CO geminate recombination in wild-type and L86A CerHbCO at pH 7.0, 20 °C.** The *smooth solid black lines* represent fits to single or double exponential functions with an offset. The gas pressure *above each solution* is marked next to each time course. There was no effect of 15 atm of xenon on geminate rebinding in wt sperm whale Mb (*WT MbCO*, *panel B*) nor was there an effect of 15 atm of N_2 on geminate recombination in wt CerHbCO (*panel A*).

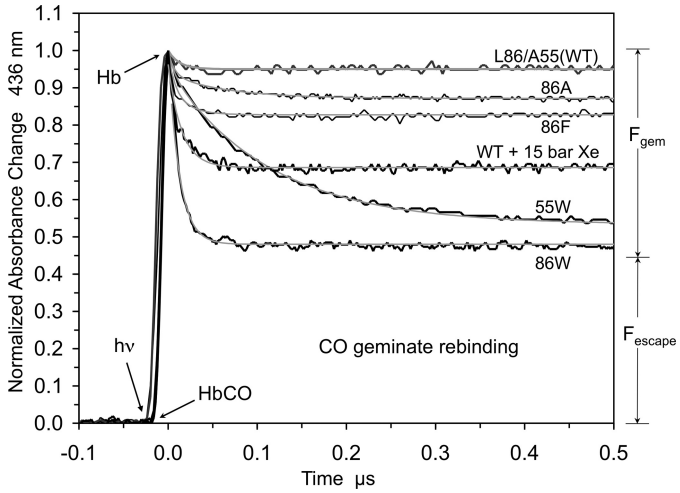

FIGURE 4. **Geminate recombination of CO in various CerHbCO mutants at pH 7.0, 20 °C.** Geminate recombination time courses for 86A (L86A), 86F (L86F), 86W (L86W), 55W (A55W), and wt CerHbCO in the presence of 15 atm of xenon are represented by *black lines*. The *smooth gray lines* represent fits to single or double exponential functions with an offset.

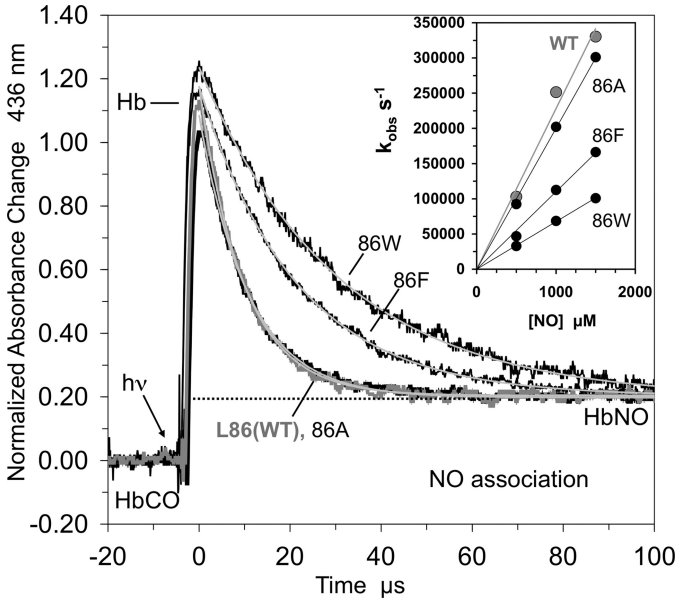

FIGURE 5. **NO binding to position 86(G12) mutants of CerHb at pH 7.0, 20 °C.** Time courses for NO binding after photolysis of 86A (L86A), 86F (L86F), 86W (L86W), and wt CerHbCO complexes at low CO concentration and high NO concentration are represented by *black lines*. The *smooth gray lines* represent fits to a single exponential function with an offset. The *inset* shows the linear dependence of k_{obs} (s^{-1}) on NO concentrations with a *y* intercept of 0.

blockage is not complete, and visual inspection of the MD simulation in time shows large movements of the Phe-86 and, to a lesser extent, the Trp-86 side chains. These fluctuations probably allow ligands to move through the restricted tunnel, even on the nanosecond time scale used in the simulations.

Molecular Dynamics of the Alternate Conformations of Gln-44(E7)—The observation of multiple Gln-44(E7) conformers in the xenon-bound L86A CerHbO$_2$ and wt aquomet CerHb structures suggests that the *out* states may partially open the E7 gate as is observed for Phe-46(CD4)Val or low pH forms of sperm whale MbCO (41, 42). MD simulations of the free energy barriers for O_2 movement were performed using the wt aquomet CerHb *in* and *out* conformers. The *in* Gln-44(E7) conformation matches that observed in wt CerHbO$_2$ (6). In simulations of the *out* conformer, the amide side chain of Gln-44(E7) is stabilized by a strong interaction between its Oϵ atom and the Nζ atom of Lys-47(E10), which occurs by an ~90° rotation of the Gln-44(E7) side chain about the Cδ-Cγ bond relative to its position for the *in* conformer in the wt aquomet CerHb crystal structure (Fig. 8*A*). However, the amide side chain still blocks the outer portion of the E7 channel.

To estimate populations and interconversion of the *in* and the *out* Gln-44(E7) conformations in wt CerHb, we performed free energy calculations for the transition in both redox states using Umbrella sampling schemes and the distance from the heme-iron atom to the Nϵ atom of Gln-44(E7) as the reaction coordinate. The *in* form is most stable in the ferrous CerHbO$_2$ state (*black line*, Fig. 8*B*), as is observed in the x-ray

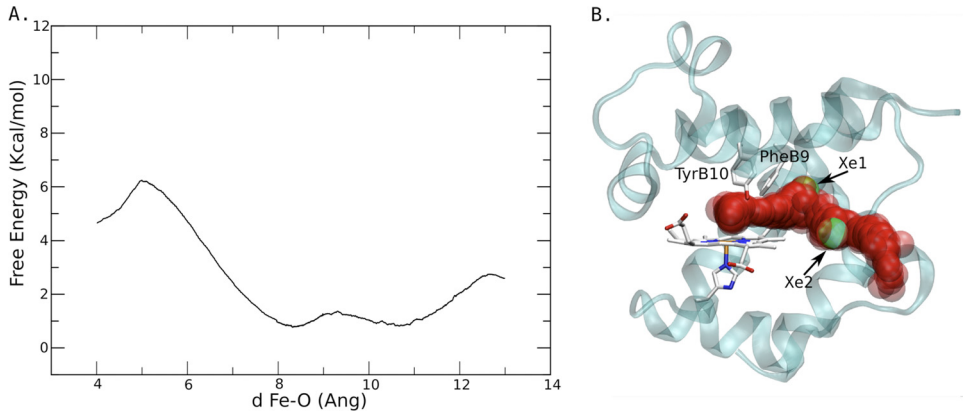

FIGURE 6. **O_2 migration in the wt CerHb channel.** *A*, free energy profile for O_2 migration. *B*, path followed by the O_2 ligand during a selected MSMD simulation. The reaction coordinate, *d*, in *panel A* is the iron to O_2 distance in Ångstroms (Ang).

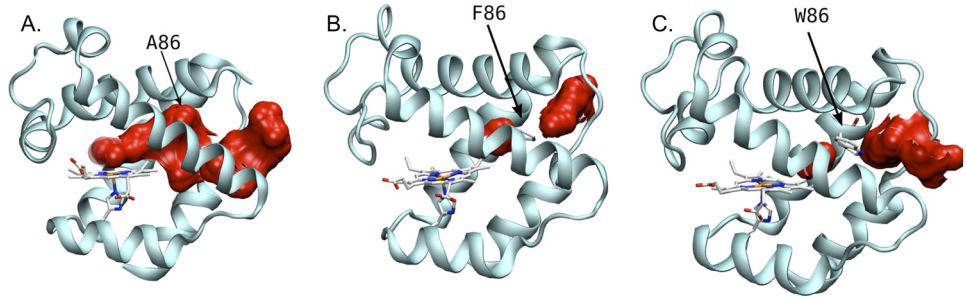

FIGURE 7. **Iso-contour energy plots associated with the ligand migration pathway in L86A, L86F, and L86W mutants of CerHb (*panels A, B, and C*, respectively).** The iso-contour energy plots were obtained for the average structure of 10-ns MD simulations.

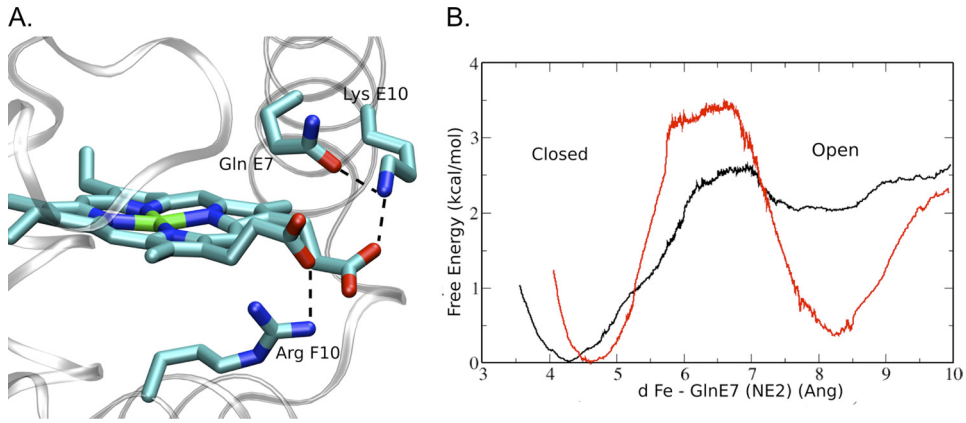

FIGURE 8. **MD simulations of the *in* to *out* Gln-44(E7) transition in wt CerHbO_2.** *A*, hydrogen-bonding interactions involving the simulated Gln-44(E7) *out* conformer and its neighboring residues are shown. *B*, free energy profile for the *in* to *out* Gln-44(E7) side-chain conformational transition. Results for the Fe^{2+} and Fe^{3+} cases are depicted using *black* and *red lines*, respectively. The reaction coordinate, *d*, in *panel B* is the iron to NE2 Gln(E7) distance in Ångstroms (Ang).

crystal structure (6). In the ferric state, the *in* and *out* conformations have similar free energy wells, explaining why both conformations are observed in the crystal structure of aquomet CerHb.

When free energy profile calculations for O_2 migration from the heme-iron to the solvent were performed using the *out* Gln-44(E7) conformation, further movement of the Gln-44(E7) side chain away from the heme-iron and out of the E7 channel occurred (Fig. 9*B*). The Nϵ and Oϵ atoms of the amide side chain are in positions similar to those seen for Nϵ and Cϵ atoms of His-64(E7) in the *open* conformation of sperm whale MbCO at low pH or in the F46V MbCO mutant (41, 42). When Gln-44(E7) is in this truly *open* conformation in CerHbCO, the calculations suggest only a small, ~1 kcal/mol, free energy barrier to ligand entry and exit through the open E7 channel (Fig. 9). These results show that the overall barrier to ligand movement through the E7 gate is governed primarily by the free energy difference between the *in* and completely *open* conformation. In the case of wt CerHbO_2 or CerHbCO, the *in* conformation of Gln-44(E7) is favored by at least a factor of 10, which probably explains why no *out* conformer is observed in the crystal structure (*i.e.* ≤10%). An additional barrier occurs for the rotation of the Gln-44(E7) side chain from the *out* conformer seen in the xenon-bound L86A CerHbO_2 and wt aquomet CerHb structures to the *open* conformer required in the simulations for O_2 exit through the E7 gate.

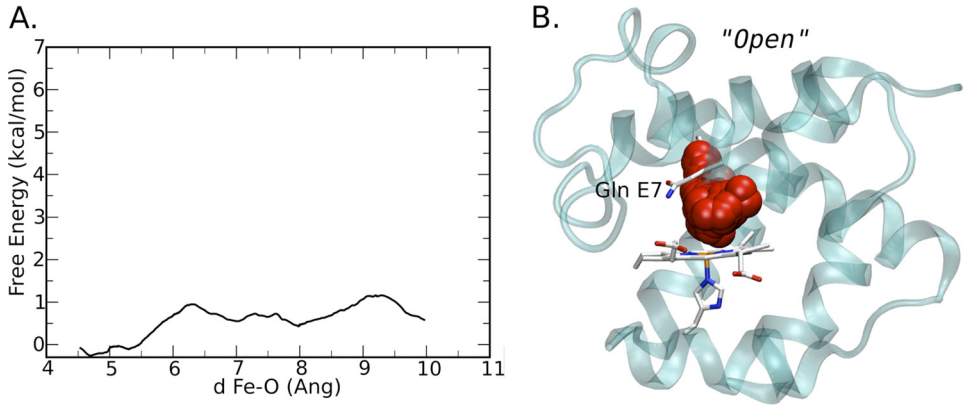

FIGURE 9. **O_2 migration through the Gln-44(E7) gate in wt CerHb.** *A*, free energy profile for O_2 migration when Gln-44(E7) occupies a hypothetical completely *open* conformation, in which the amide side chain has rotated even further away from the heme-iron than in the *out* conformation shown in Fig. 8. *B*, path followed by the O_2 ligand during a selected MSMD simulation for the hypothetical *open* conformer. The reaction coordinate, *d*, in *panel A* is the iron to O_2 distance in Ångstroms (Ang).

DISCUSSION

The Size and Accessibility of the Apolar Channel—The crystal structure of L86A CerHbO_2 equilibrated with ~10 atm of xenon demonstrates that the central cavity between the E and H helices is readily accessible to apolar gases (Fig. 1). The exact positions of Xe1 and Xe2 are near the free energy wells calculated for wt CerHbO_2 using dioxygen as a probe (Fig. 6). Xenon binding to both wt and L86A CerHbCO causes a significant increase of F_{gem} (Fig. 3), experimentally demonstrating that occupancy of the apolar cavity blocks ligand escape. Even though xenon binding to animal Hbs and Mbs is well documented, the results for CerHb are the first to show a large effect on the fraction of geminate recombination and that the xenon cavities are on the pathway for ligand entry and escape. In contrast, xenon binding to sperm whale Mb and *S. inaequivalvis* Hb causes little or no change in F_{gem} for either O_2 or CO rebinding (13, 18, 19).

The extent of geminate recombination also increases significantly, to ~50%, when the size of the Leu-86(G12) side chain is increased (Fig. 4). The L86F and L86W mutations cause marked decreases in both k'_{O_2} and k_{O_2} with little change in affinity as would be expected if the pathways for ligand entry and exit were blocked (Table 4). The magnitude of the L86W effect is similar to that observed when exit from the tunnel into the solvent is blocked by the A55W mutation (Fig. 4, Table 4, and Ref. 2). The tunnel mutations also cause large decreases (4–5-fold) of the rate constant for bimolecular NO binding, which is limited only by movement into the protein (Table 5). Similar decreases are obtained for the bimolecular rate constant for ligand entry calculated using k'_{CO}, F_{gem}, and Equation 1 (Table 5).

Pathway for Ligand Binding—As described above, filling the apolar cavity with either xenon atoms or large aromatic amino acids at position 86(G12) markedly inhibits ligand entry and exit and increases both the rate and extent of geminate recombination. The simplest interpretation of these results is shown in Scheme 1 (2, 7). The apolar tunnel containing the xenon binding sites is assumed to be the major pathway for ligand entry and escape. Laser excitation photodissociates the iron-ligand bond, generating an initial intermediate with ligand remaining in the distal pocket (state B). From there the ligand either rebinds rapidly or moves into the apolar tunnel. Once inside the tunnel, the ligand can occupy multiple locations in the large space between the distal pocket and the solvent aperture. This large space slows return to the heme-iron and geminate recombination, allowing most of the ligands to escape into solvent.

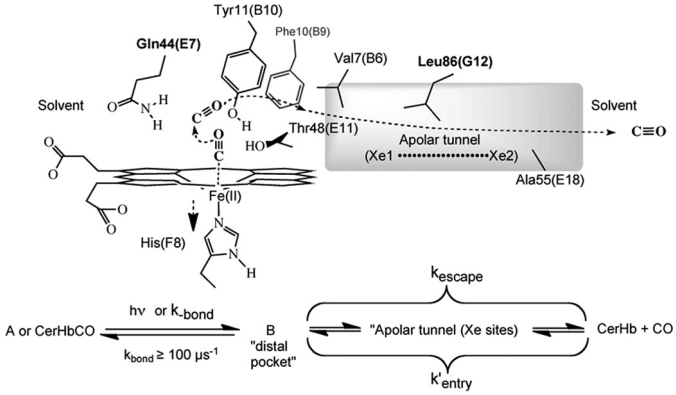

SCHEME 1

When xenon atoms or the indole ring of Trp-86(G12) block the initial portion of the tunnel, ligands are trapped in or very near to the distal pocket and rapidly rebind to the heme iron. As a result, large values of k_{gem} and F_{gem} are observed (Fig. 4, Tables 3 and 5). The ligand molecules that move past the bound xenon atoms or the Trp-86(G12) side chain rapidly escape because return to the distal heme pocket from the exterior portion of the tunnel is restricted. When the tunnel exit is blocked by the A55W mutation, F_{gem} also increases. However, in this case, the rate of internal rebinding decreases markedly because the trapped ligand molecules can access the entire apolar tunnel, making return to the heme iron and net escape much slower (Fig. 4 and Table 5). Scheme 1 is also supported strongly by the calculations shown in Fig. 6. Entry into the tunnel has a free energy barrier of ~5.5 kcal/mol due to steric restrictions by Phe-10(B9), Tyr-11(B10), Thr-48(E11), and Val-7(B6) (Scheme 1). The steric barrier between the two xenon sites (near Leu-86) is small (≤1 kcal/mol), and the exit to solvent is near Ala-55, with a barrier of ~2 kcal/mol.

This mechanism also explains the results for the L86A mutation. Even though the steric barrier is small in wt CerHbCO, the Leu-86(G12) side chain does separate the two xenon binding sites (Fig. 6). As a result, ligands are partially sequestered close to the distal pocket, causing the small amount of observed geminate rebinding to be fast in wt CerHbCO. At the same time, the Leu-86(G12) restriction decreases F_{gem} by inhibiting ligand return to the distal pocket from the more exterior portions of the tunnel. When Ala replaces Leu at this position, geminate recombination is biphasic. The observed time course shows a small rapid phase with $F_{gem} = 0.05$ and $k_{gem} \geq 100\ \mu s^{-1}$, values that are similar to those for wt CerHbCO, and a second, slow phase with $F_{gem} \approx 0.05$ and $k_{gem} \approx 15\ \mu s^{-1}$. The latter slower phase represents ligand return from the exterior portion of the tunnel, presumably the Xe2 site, at a rate similar to that seen for geminate recombination in the A55W mutant, whereas the fast phase represents rapid ligand rebinding from the Xe1 site as is observed in wt CerHb.

Conformational Flexibility of Gln-44 and the Role of the E7 Gate—In the crystal structure of wt $CerHbO_2$, the amide side chain of Gln-44(E7) appears to be fixed in position by multiple hydrogen bonding interactions with the bound ligand and the hydroxyl groups of Tyr-11(B10) and Thr-48(E11). However, when the structure of A55W $CerHbO_2$ was examined in detail (2), two conformations for the Gln-44(E7) side chain were observed that differed primarily by rotation about the Cα-Cβ bond. In the *in* conformation the amide Nϵ atom donates a hydrogen bond to the bound ligand, whereas in the *out* orientation the amide side chain interacts with the carbonyl of Ala-40(E3) and the heme propionates through well defined crystallographic water molecules. Two similar Gln-44(E7) conformations occur in the xenon-bound L86A $CerHbO_2$ and wt aquomet CerHb structures (Fig. 2). These structures suggest that the Gln-44(E7) side chain is not rigidly held in place but may fluctuate between positions in which the amide side chain interacts electrostatically with either internal polar side chains and bound ligand or with Lys-47(E10), the carbonyl O atom of Ala-40(E3), the heme propionates, and water molecules at the solvent interface.

Simulation of the interconversion between the *in* and *out* conformers in the wt $CerHbO_2$ and aquomet CerHb structures suggests a free energy barrier of 2.5 to 3.5 kcal/mol (Fig. 8). The *out* conformer appears to be ≥2 kcal/mol less stable than the *in* conformation in $CerHbO_2$. MD simulations of the *out* conformer of wt $CerHbO_2$ leads to a modified orientation in which the amide Oϵ atom of Gln-44(E7) directly accepts a proton from the side chain of Lys-47(E10), which in turn interacts electrostatically with the heme A propionate. However, even in this *out* conformation, the Gln-44(E7) side chain still blocks the access to the heme-iron through the E7 gate.

A simulation of ligand migration through the E7 gate when Gln-44(E7) is initially in the *out* conformer is shown in Fig. 9*A*. To allow ligand escape from the E7 channel, the Gln-44(E7) side chain must rotate further by ~180° about the Cβ-Cγ bond, which moves the amide atoms away from the heme plane and up against Phe-25(CD1) and Phe-27(CD3), pushing the benzyl rings away from the heme group. When the Gln-44(E7) residue is in this completely *open* conformation, the free energy barrier to ligand movement through the E7 gate is very small compared with the free energy difference and barrier between the *in* and *out* conformers in the reduced state (Figs. 9*A* *versus* 8*B*). The latter differences plus the free energy required to rotate the Gln-44(E7) side chain into the completely *open* conformation determine the kinetic barrier to ligand escape through the E7 gate, which must be ≥4 kcal/mol and is probably much higher than the ~6 kcal/mol barrier estimated for ligand movement into the apolar channel from the distal pocket shown in Fig. 6*A*.

When Gln-44(E7) is replaced with small amino acid side chains, there are no changes in the rates of O_2, CO, and NO binding or in the fractions of either O_2 or CO geminate recombination (2). The Q44F and Q44W mutations do cause 10-fold decreases in the rates of ligand association, but the rates of dissociation stay the same or increase 2-fold. As a result, these mutations cause marked 10-fold decreases in ligand affinity. The decreases in the association rate constants appear to be due to direct steric hindrance of internal iron-ligand bond formation by the large aromatic side chains and not to a change in the rate of ligand entry and escape. This conclusion is supported by the lack of an increase in the fraction of CO geminate recombination when the size of the amino acid at position 44(E7) is increased progressively from Ala to Trp, and F_{gem} remains at 0.05–0.1 for all the Gln-44(E7) mutants (Fig. 3 in Ref. 2).

In contrast, the L86W and A55W mutations and xenon binding within the apolar channel cause large increases in $F_{gem,CO}$ after laser photolysis (Figs. 3, 4, and 5). These effects are unambiguous, indicate that the apolar tunnel is the major pathway for ligand movement into the protein, and demonstrate that the side chains at positions 86(G12) and 55(E18) line the major pathway for ligand entry and exit.

However, the Trp tunnel mutations do not completely inhibit ligand binding. The observed bimolecular rate constants for ligand entry into the L86W and A55W mutants (k'_{NO} and k'_{entry} values, Table 4) are 30–60 $\mu M^{-1}s^{-1}$, which although ~4-fold less than the wt CerHb values, are similar to the values for both wt and His(E7)Gln mutants of sperm whale Mb (13) and the α and β subunits of human HbA (14). Thus, ~25% of the ligand molecules could be entering the active site of CerHb through the E7 gate as shown in Fig. 9*B*, and the motions of the Gln-44(E7) side chain shown in Figs. 2, 8, and 9 are very similar to those seen for opening of the His(E7) gate in mammalian Mbs and Hbs (41, 42).

The 4–5-fold higher rates of ligand entry observed for native CerHb are due to the evolution of an unhindered apolar tunnel, which results from the loss of the A-helix and replacement of large amino acid side chains with small ones between the E- and H-helices. The lower net barrier for entry into the active site through this tunnel is due to elimination of the need for large conformational changes to open the E7 gate and to favorable partitioning of apolar diatomic gases into the large pre-existing tunnel, which effectively pre-concentrates the ligand for movement into the heme pocket. Similar unhindered, continuous apolar channels are not found in mammalian Mbs and Hbs, which accounts for why the E7 channel appears to be the dominant pathway even though the barrier

to complete opening of the distal histidine or glutamine gate is significant.

REFERENCES

1. Elber, R. (2010) *Curr. Opin. Struct. Biol.* **20,** 162–167
2. Salter, M. D., Nienhaus, K., Nienhaus, G. U., Dewilde, S., Moens, L., Pesce, A., Nardini, M., Bolognesi, M., and Olson, J. S. (2008) *J. Biol. Chem.* **283,** 35689–35702
3. Geuens, E., Dewilde, S., Hoogewijs, D., Pesce, A., Nienhaus, K., Nienhaus, G. U., Olson, J., Vanfleteren, J., Bolognesi, M., and Moens, L. (2004) *IUBMB Life* **56,** 653–656
4. Bolognesi, M., Bordo, D., Rizzi, M., Tarricone, C., and Ascenzi, P. (1997) *Prog. Biophys. Mol. Biol.* **68,** 29–68
5. Vandergon, T. L., Riggs, C. K., Gorr, T. A., Colacino, J. M., and Riggs, A. F. (1998) *J. Biol. Chem.* **273,** 16998–17011
6. Pesce, A., Nardini, M., Dewilde, S., Geuens, E., Yamauchi, K., Ascenzi, P., Riggs, A. F., Moens, L., and Bolognesi, M. (2002) *Structure* **10,** 725–735
7. Deng, P., Nienhaus, K., Palladino, P., Olson, J. S., Blouin, G., Moens, L., Dewilde, S., Geuens, E., and Nienhaus, G. U. (2007) *Gene* **398,** 208–223
8. Hundahl, C., Fago, A., Dewilde, S., Moens, L., Hankeln, T., Burmester, T., and Weber, R. E. (2006) *FEBS J.* **273,** 1323–1329
9. Martí, M. A., Bikiel, D. E., Crespo, A., Nardini, M., Bolognesi, M., and Estrin, D. A. (2006) *Proteins* **62,** 641–648
10. Pesce, A., Nardini, M., Ascenzi, P., Geuens, E., Dewilde, S., Moens, L., Bolognesi, M., Riggs, A. F., Hale, A., Deng, P., Nienhaus, G. U., Olson, J. S., and Nienhaus, K. (2004) *J. Biol. Chem.* **279,** 33662–33672
11. Draghi, F., Miele, A. E., Travaglini-Allocatelli, C., Vallone, B., Brunori, M., Gibson, Q. H., and Olson, J. S. (2002) *J. Biol. Chem.* **277,** 7509–7519
12. Mims, M. P., Porras, A. G., Olson, J. S., Noble, R. W., and Peterson, J. A. (1983) *J. Biol. Chem.* **258,** 14219–14232
13. Scott, E. E., Gibson, Q. H., and Olson, J. S. (2001) *J. Biol. Chem.* **276,** 5177–5188
14. Birukou, I., Schweers, R. L., and Olson, J. S. (2010) *J. Biol. Chem.* **285,** 8840–8854
15. de Sanctis, D., Dewilde, S., Pesce, A., Moens, L., Ascenzi, P., Hankeln, T., Burmester, T., and Bolognesi, M. (2004) *Biochem. Biophys. Res. Commun.* **316,** 1217–1221
16. Milani, M., Pesce, A., Ouellet, Y., Dewilde, S., Friedman, J., Ascenzi, P., Guertin, M., and Bolognesi, M. (2004) *J. Biol. Chem.* **279,** 21520–21525
17. Raushel, F. M., Thoden, J. B., and Holden, H. M. (2003) *Acc. Chem. Res.* **36,** 539–548
18. Knapp, J. E., Pahl, R., Cohen, J., Nichols, J. C., Schulten, K., Gibson, Q. H., Srajer, V., and Royer, W. E., Jr. (2009) *Structure* **17,** 1494–1504
19. Scott, E. E., and Gibson, Q. H. (1997) *Biochemistry* **36,** 11909–11917
20. Pesce, A., Nardini, M., Dewilde, S., Ascenzi, P., Riggs, A. F., Yamauchi, K., Geuens, E., Moens, L., and Bolognesi, M. (2001) *Acta Crystallogr. D Biol. Crystallogr.* **57,** 1897–1899
21. Evans, P. R. (1993) *Proceedings of the CCP4 Study Weekend on Data Collection and Processing*, pp. 114–122, CLRC Daresbury Laboratory, Warrington, UK
22. Leslie, A. G. M. (2003) MOSFLM User Guide, Mosflm Version 6.2.3. (Laboratory of Molecular Biology) Cambridge, UK
23. Vagin, A. A., and Teplyakov, A. (1997) *J. Appl. Crystallogr.* **30,** 1022–1025
24. Murshudov, G. N., Vagin, A. A., and Dodson, E. J. (1997) *Acta Crystallogr. D Biol. Crystallogr.* **53,** 240–255
25. Emsley, P., and Cowtan, K. (2004) *Acta Crystallogr. D Biol. Crystallogr.* **60,** 2126–2132
26. Laskowski, R. A., MacArthur, M. W., Moss, D. S., and Thornton, J. M. (1993) *J. Appl. Crystallogr.* **26,** 283–291
27. Laskowski, R. A. (1995) *J. Mol. Graph.* **13,** 323–330
28. Berman, H. M., Westbrook, J., Feng, Z., Gilliland, G., Bhat, T. N., Weissig, H., Shindyalov, I. N., and Bourne, P. E. (2000) *Nucleic Acids Res.* **28,** 235–242
29. Wang, J., Cieplak, P., and Kollman, P. A. (2000) *J. Comput. Chem.* **21,** 1049–1074
30. Pearlman, D. A., Case, D. A., Caldwell, J. W., Ross, W. R., Cheatham, T. E., III, DeBolt, S., Ferguson, D., Seibel, G., and Kollman, P. A. (1995) *Comp. Phys. Commun.* **91,** 1–41
31. Bayly, C. I., Cieplak, P., Cornell, W., and Kollman, P. A. (1993) *J. Phys. Chem.* **97,** 10269–10280
32. Marti, M. A., Crespo, A., Capece, L., Boechi, L., Bikiel, D. E., Scherlis, D. A., and Estrin, D. A. (2006) *J. Inorg. Biochem.* **100,** 761–770
33. Jarzynski, C. (1997) *Phys. Rev. Lett.* **78,** 2690–2693
34. Leach, A. R. (2001) *Molecular Modelling Principles and Applications,* 2nd Ed., pp. 581–582, Pearson Education Limited, Edinburgh Gate, England
35. Martí-Renom, M. A., Stuart, A. C., Fiser, A., Sánchez, R., Melo, F., and Sali, A. (2000) *Annu. Rev. Biophys. Biomol. Struct.* **29,** 291–325
36. Moschetti, T., Mueller, U., Schulze, J., Brunori, M., and Vallone, B. (2009) *Biophys. J.* **97,** 1700–1708
37. Schoenborn, B. P. (1965) *Nature* **208,** 760–762
38. Schoenborn, B. P., Watson, H. C., and Kendrew, J. C. (1965) *Nature* **207,** 28–30
39. Tilton, R. F., Jr., Kuntz, I. D., Jr., and Petsko, G. A. (1984) *Biochemistry* **23,** 2849–2857
40. Savino, C., Miele, A. E., Draghi, F., Johnson, K. A., Sciara, G., Brunori, M., and Vallone, B. (2009) *Biopolymers* **91,** 1097–1107
41. Lai, H. H., Li, T., Lyons, D. S., Phillips, G. N., Jr., Olson, J. S., and Gibson, Q. H. (1995) *Proteins* **22,** 322–339
42. Yang, F., and Phillips, G. N., Jr. (1996) *J. Mol. Biol.* **256,** 762–774